

ARTICLE

<https://doi.org/10.1038/s41467-019-12569-9>

OPEN

Two-dimensional inorganic molecular crystals

Wei Han^{1,4}, Pu Huang^{2,4}, Liang Li¹, Fakun Wang¹, Peng Luo¹, Kailang Liu¹, Xing Zhou¹, Huiqiao Li^{1,3},
Xiuwen Zhang², Yi Cui^{3*} & Tianyou Zhai^{1*}

Two-dimensional molecular crystals, consisting of zero-dimensional molecules, are very appealing due to their novel physical properties. However, they are mostly limited to organic molecules. The synthesis of inorganic version of two-dimensional molecular crystals is still a challenge due to the difficulties in controlling the crystal phase and growth plane. Here, we design a passivator-assisted vapor deposition method for the growth of two-dimensional Sb_2O_3 inorganic molecular crystals as thin as monolayer. The passivator can prevent the heterophase nucleation and suppress the growth of low-energy planes, and enable the molecule-by-molecule lateral growth along high-energy planes. Using Raman spectroscopy and in situ transmission electron microscopy, we show that the insulating α -phase of Sb_2O_3 flakes can be transformed into semiconducting β -phase under heat and electron-beam irradiation. Our findings can be extended to the controlled growth of other two-dimensional inorganic molecular crystals and open up opportunities for potential molecular electronic devices.

¹State Key Laboratory of Material Processing and Die & Mould Technology, School of Materials Science and Engineering, Huazhong University of Science and Technology (HUST), 430074 Wuhan, China. ²Shenzhen Key Laboratory of Flexible Memory Materials and Devices, College of Electronic Science and Technology, Shenzhen University, Nanhai Avenue 3688, 518060 Shenzhen, Guangdong, China. ³Department of Material Science and Engineering, Stanford University, 94305 Stanford, CA, USA. ⁴These authors contributed equally: Wei Han, Pu Huang. *email: yicui@stanford.edu; zhaity@hust.edu.cn

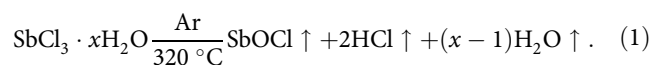
Molecular clusters, composed of molecules instead of atoms as building blocks, enable the design of functional materials from the bottom-up with unique and customized properties^{1,2}. Assembled by molecular clusters, two-dimensional molecular crystals (2DMCs) with in-plane intermolecular van der Waals (vdW) forces have emerged as the promising materials for next-generation electronics because of their quantum tunneling effect, tunable properties by molecular design, dangling-bond-free surface, and molecularly uniform thinness³. Recently, 2DMCs have achieved some novel phenomena such as breaking the Landauer limit in a molecular diode⁴, Peltier cooling at molecular scale⁵, molecular spinterface⁶, and humidity-controlled rectification switching⁷. Nevertheless, most 2DMCs currently studied are self-assembled films of complex organic molecules and only limited to growth on hydroxyl-groups terminated substrate, generally with molecular defects and thermal-instability, impacting device performance⁸. Zero-dimensional (0D) inorganic molecules are more stable candidates with simple structures⁹, which have applications in diverse fields, such as spin-photovoltaic¹⁰, optoelectronic¹¹, and field-effect transistors¹². The library of 0D inorganic molecules includes C₆₀, metal-halide perovskites, and metal chalcogenides, and they have been widely explored in the form of quantum dots and thin films^{1,11,13}. Unfortunately, two-dimensional inorganic molecular crystals (2DIMCs) have seldom been studied. Due to the miniaturization and integration trends in the electronic industry, the reliable synthesis of large-area and high-quality 2DIMCs is crucial. However, due to the insolubility of inorganic molecules, it is difficult to obtain large-size self-assembled 2DIMCs.

Recently, C₆₀-based inorganic nanosheets were obtained via mechanical exfoliation from layered solid, but the yield is limited and the thickness is uncontrollable¹⁴, which hampered further research. By contrast, vapor deposition can produce high-quality 2D inorganic atomic crystals with controllable size and thickness^{15–19}. In this process, inorganic sources grow into 2D crystals via atom-by-atom reaction and then layer-by-layer growth along a preferential crystal orientation with the lowest surface energy. Unfortunately, the molecule-by-molecule growth of 2DIMCs however turns to be much less preferential due to the weaker crystalline anisotropy, where the molecules, from all orientations, are bonded via the van der Waals forces. The absence of orientation preference thus results in the difficulties of growing in a 2D way. This growth tendency can be verified by the previous report²⁰, in which 0D molecules tend to spontaneously assemble to 1D rods instead of 2D flakes or sheets. Therefore, the conventional vapor deposition approach is still very hard for the growth of 2DIMCs. In the growth mechanism of vapor deposition, the vapor-phase precursors are converted to a solid-state crystal via surface nucleation, surface diffusion, and crystal growth¹⁸, and thus the growth plane is determined primarily by the surface nucleation stage. The high-energy planes usually grow preferentially and low-energy planes will be inhibited. Therefore, controlling the crystal plane of nucleation is the key for the synthesis of 2DIMCs.

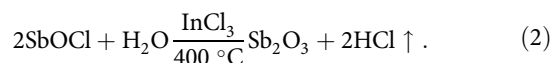
Herein, we report the synthesis of ultrathin 2D Sb₂O₃ molecular crystals with thickness down to monolayer on mica substrates by passivator-assisted vapor deposition (PAVD). The passivator is found to play a key role in controlling the crystal phase and promoting the growth of Sb₂O₃ molecular crystals in a preferential orientation. Both in-situ and ex-situ Raman spectroscopy reveal that Sb₂O₃ flakes exhibit a heat-induced reversible structural phase transition. Using in-situ TEM, we have observed that Sb₂O₃ flakes undergo an $\alpha \rightarrow \beta$ structural transition under electron-beam irradiation. Our findings provide the growth strategy of 2DIMCs and the mechanism of structural transition, and demonstrate their potential applications in phase-change devices.

Results

Growth of 2D Sb₂O₃ molecular crystals. Here, 2D Sb₂O₃ molecular crystals were successfully prepared on atomically flat mica substrates by InCl₃-assisted (Route 1) and Se-assisted (Route 2) PAVD growth process in a three-zone tube furnace, as depicted in the schematic diagram in Fig. 1a. The 2D Sb₂O₃ flakes possess a cubic cell ($a = b = c = 11.15 \text{ \AA}$, space group *Fd-3m*) composed of spherical Sb₄O₆ adamantoid cages connected by vdW forces²¹ in contrast to the well-known 2D materials (Graphene, MoS₂)^{18,19}, which are bonded via the in-plane covalent bonds (Fig. 1b). Within these Sb₄O₆ molecular cages, each O atom is connected by two Sb atoms, while each Sb atom is bonded with three O atoms. Figure 1c illustrates the schematic of PAVD growth of 2D Sb₂O₃ flakes. In Route 1, hydrophilic SbCl₃·xH₂O was chosen as the precursor, which undergoes the following reaction to supply the vapor of intermediate SbOCl²².



The SbOCl and H₂O react to become Sb₂O₃ under the passivation effect of InCl₃.



The passivation effect of InCl₃ is demonstrated by a series of experiments by varying the amount of InCl₃ in this chemical vapor deposition (CVD) growth process (see Supplementary Fig. 1). Without the passivation effect of InCl₃, Sb₂O₃ tends to form thick rods. By fine tuning the amount of InCl₃, the growth of low-energy crystal planes is suppressed, and the high-energy planes are promoted, leading to the formation of ultrathin Sb₂O₃ flakes. The passivation effect of Se in Route 2 and growth mechanism will be discussed in detail afterwards. Figure 1d, e presents the typical optical images of ultrathin triangular Sb₂O₃ flakes deposited on mica by Route 1 and Route 2, respectively, with thickness down to monolayer and lateral size of over 20 μm . The lateral size, thickness, and nucleation density of Sb₂O₃ flakes can be controlled by the position of mica substrates (Supplementary Fig. 2). The maximum lateral size of a triangular Sb₂O₃ flake is 23 μm (Fig. 1f). The representative AFM images of monolayer (1L), bilayer (2L), and trilayer (3L) Sb₂O₃ flakes are shown in Fig. 1g–i (more AFM images are shown in Supplementary Fig. 3). It is noted that the height of a monolayer Sb₂O₃ flake is about 0.64 nm, consistent with the theoretical thickness of 6.4 \AA of single-molecule layer²³. Furthermore, this PAVD method can be extended to the growth of other molecular crystals, such as SbI₃ (Supplementary Fig. 4)²⁴.

To identify the crystal phase and quality of as-grown Sb₂O₃ flakes, Raman spectroscopy was carried out using a 532 nm excitation laser. The primitive cell of bulk Sb₂O₃ (space group *Fd-3m*, No. 227) consists of two formula units of Sb₄O₆ and 20 atoms, and thus there are 20 \times 3 vibrational modes at the Γ point in Brillouin zone (BZ):

$$\Gamma = 2A_g + 2A_u + 2E_u + 2E_g + 3F_{2u} + 5F_{2g} + 5F_{1u} + 3F_{1g},$$

where 2A_g, 2E_g, and 5F_{2g} modes are Raman active²¹. One of them is a translational F_{2g} mode at lower frequency (81 cm⁻¹) and the rest are internal modes within the Sb₄O₆ adamantoid cage. As shown in Fig. 1j, ¹F_{2g}, ²F_{2g}, ¹A_g, and ²A_g modes are observed in both ultrathin and bulk Sb₂O₃. The Raman spectra of 2D Sb₂O₃ flakes with different thicknesses and bulk Sb₂O₃ reveal a layer-dependent blueshift trend of every peak frequency with decreasing thickness. Compared with the Raman spectrum of bulk Sb₂O₃ (²F_{2g} ~ 188.8 cm⁻¹, ¹A_g ~ 252.9 cm⁻¹), there is a clear trend that both ²F_{2g} peak and ¹A_g peak move to the higher wavenumber

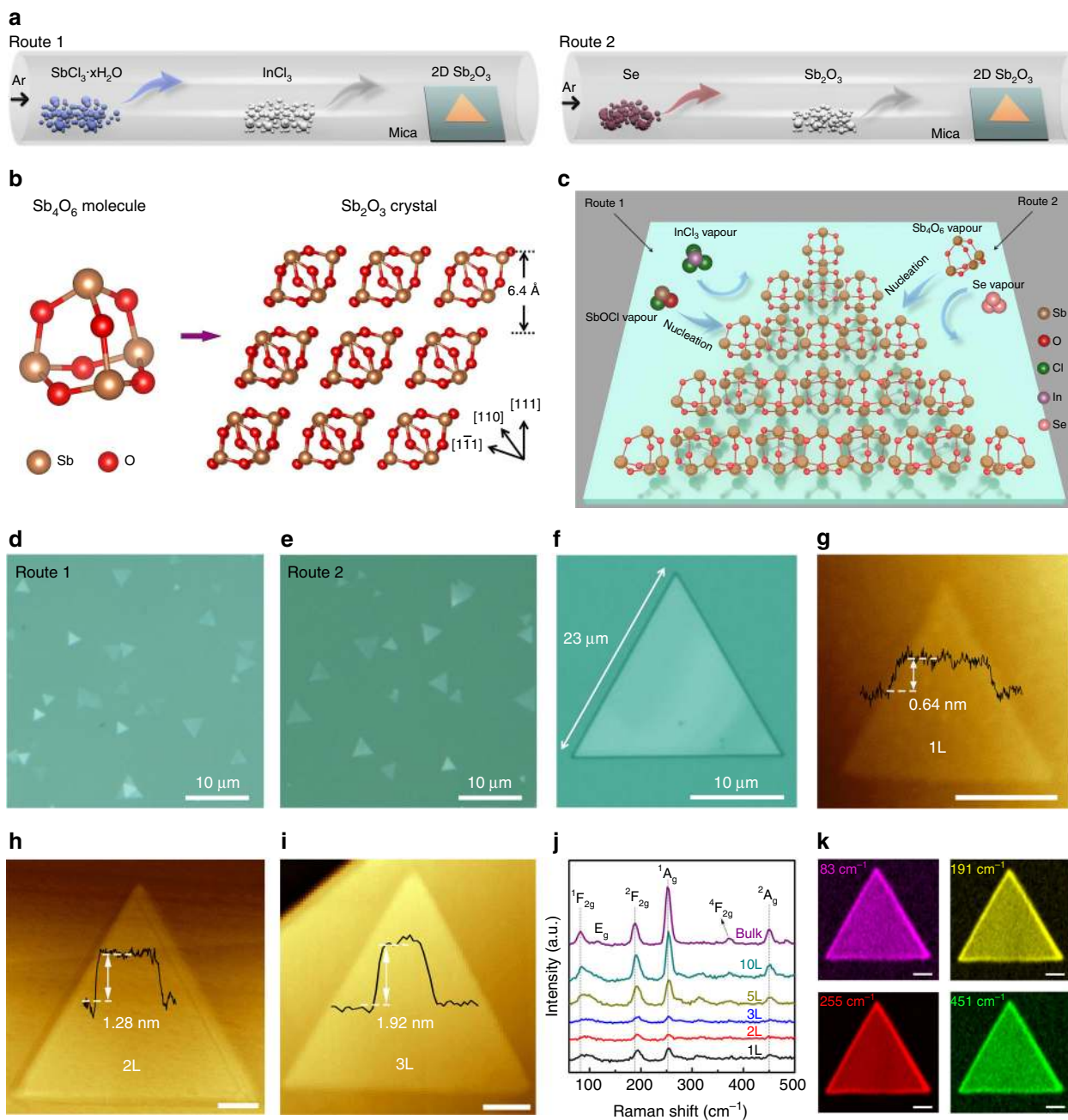


Fig. 1 PAVD growth of 2D Sb_2O_3 molecular crystals. **a** Schematic diagram of passivator-assisted vapor deposition (PAVD) growth of Sb_2O_3 flakes in a tube furnace. In Route 1, precursor $\text{SbCl}_3 \cdot x\text{H}_2\text{O}$, undergo a chemical reaction and grow to Sb_2O_3 flakes on mica with the assistance of passivator InCl_3 . In Route 2, precursor Sb_2O_3 become gaseous, and grow to Sb_2O_3 flakes assisted by passivator Se. **b** Ball-and-stick structural models of spherical Sb_4O_6 molecule and Sb_2O_3 molecular crystal. **c** Schematic of PAVD growth of 2D Sb_2O_3 molecular crystals on mica. The reaction involves: (1) nucleation of Sb_2O_3 clusters from decomposition of SbOCl vapor (Route 1) and adsorption of Sb_4O_6 vapor (Route 2); (2) adsorption of passivators; (3) horizontal growth of Sb_2O_3 flakes along the mica surface. **d, e** Optical images of ultrathin triangular Sb_2O_3 flakes deposited on mica by Route 1 and Route 2. **f** Optical image of a triangular Sb_2O_3 flake as large as $\sim 23 \mu\text{m}$. **g–i** Representative AFM images of monolayer (1L), bilayer (2L), and trilayer (3L) Sb_2O_3 flakes. Scale bars, 200 nm. **j** Layer-dependent Raman spectra of Sb_2O_3 flakes from 1L to bulk. **k** Spatially resolved Raman mapping images of an Sb_2O_3 flake at four peak frequencies 83, 191, 255, and 451 cm^{-1} . Color scales, black to colorized, low to high Raman intensity. Scale bars, 2 μm

region ($^2\text{F}_{2g} \sim 194.0 \text{ cm}^{-1}$, $^1\text{A}_g \sim 255.5 \text{ cm}^{-1}$) for monolayer Sb_2O_3 . Such a blueshift could be a result of the decreased long-range Coulombic intramolecular interactions in thinner flakes²⁵. The relation between frequency and number of layers for $^2\text{F}_{2g}$ peak and $^1\text{A}_g$ peak is plotted in Supplementary Fig. 5a, showing a monotonic decrease trend of frequency with increasing layer number. The molecular vibrations of four Raman modes are illustrated in Supplementary Fig. 5b. The $^1\text{F}_{2g}$ mode is an

intermolecular mode and the others are intramolecular ones. The $^1\text{A}_g$ mode is from Sb–O–Sb stretch mode while $^2\text{F}_{2g}$ and $^2\text{A}_g$ are classified into Sb–O–Sb bend modes. The spatially resolved Raman mapping images at four peak frequencies (83, 191, 255, and 451 cm^{-1}) reveal the uniform triangular domain of the Sb_2O_3 crystal (Fig. 1k).

Figure 2a, b illustrates the top-view ball-and-stick models of monolayer and trilayer Sb_2O_3 flakes with (111) plane, which is the

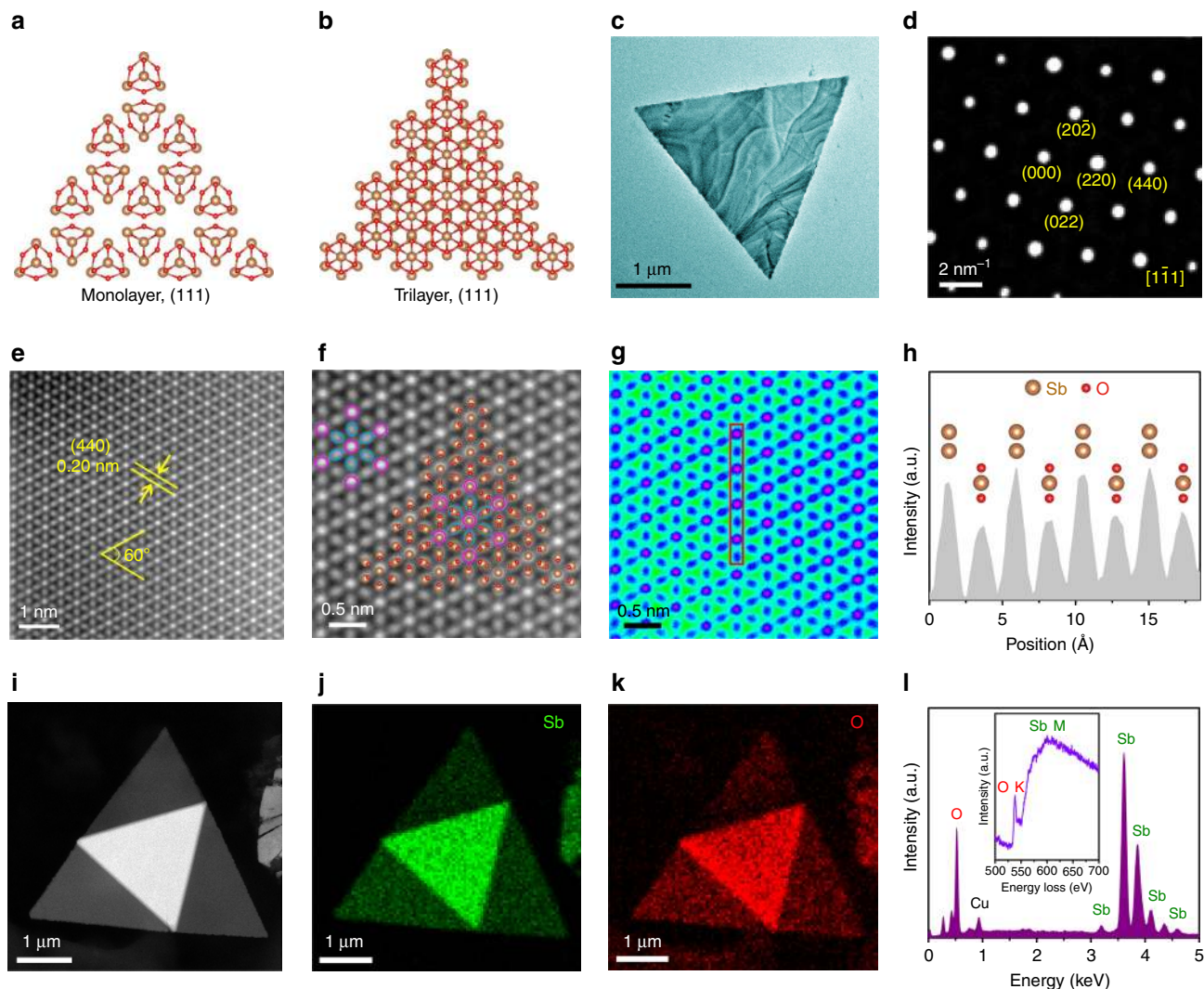


Fig. 2 Atomic structure of 2D Sb_2O_3 molecular crystals. **a, b** Top-view structural models of monolayer and trilayer Sb_2O_3 flakes with (111) plane. Brown balls, Sb atoms. Red balls, O atoms. **c** TEM image of a triangular Sb_2O_3 flake. **d** SAED pattern of the Sb_2O_3 flake. **e** Z-contrast atomic-level HAADF-STEM image of the Sb_2O_3 flake showing the perfect atomic lattice. **f** Enlarged HAADF image and the matched atomic ball model, white atoms are marked by yellow circles and gray atoms are marked by blue circles. **g** Scattered electron intensity color image for (f). **h** Intensity line profile along the red box in (g). **i–k** HAADF image of a stacked flake and the corresponding elemental maps for Sb and O. **l** EDX and EELS spectra of the Sb_2O_3 flake

most close-packed layered crystal plane and has the lowest surface energy for face-centered cubic (FCC) Sb_2O_3 . As shown in Fig. 2c, d, the transmission electron microscope (TEM) image and selected area electron diffraction (SAED) pattern reveal that the triangular Sb_2O_3 flake is a high-quality single crystal with (111) top plane, which belongs to {111} crystal plane family. The specific atomic structure of Sb_2O_3 flake was verified by aberration-corrected high-angle annular dark-field scanning transmission electron microscope (HAADF-STEM). Figure 2e demonstrates the typical Z-contrast atomic-level HAADF image of an ultrathin Sb_2O_3 flake, which reveals a quasi hexagonal close-packed (HCP) structure arrangement of white and gray atoms with crystal plane distance of 0.2 nm corresponding to (440) plane of Sb_2O_3 . Figure 2f demonstrates the enlarged HAADF image and the matched atomic ball model, where the brighter round spots marked by red circles represent the Sb atomic columns (red spots in Fig. 2g) and the dimmer elliptic spots marked by blue circles are the staggered O-Sb-O atomic columns (blue spots in Fig. 2g). This lattice pattern can be further verified by the intensity line profile along the red box (Fig. 2h). According to the intensity ratio, the strong peaks represent the two stacked

Sb atoms and the weak peaks are the O-Sb-O atoms. We used energy dispersive X-ray spectroscopy (EDS) and electron energy-loss spectroscopy (EELS) to identify the chemical composition of the flakes. The elemental maps for Sb and O of a stacked flake in Fig. 2i–k show the uniform distribution of Sb and O elements. EDS and EELS spectra in Fig. 2l indicate that the as-grown Sb_2O_3 flakes are composed of Sb and O.

In order to investigate the growth mechanism, the samples obtained by adding different amounts of passivators were characterized. Taking Se as an example (the data about InCl_3 is shown in Supplementary Fig. 1), Sb_2O_3 samples with different morphology were obtained under different amounts of Se. As shown in Fig. 3a–h, the morphology of Sb_2O_3 is transformed from submicronwires (522 nm) to thick triangle flakes (76 nm), and then is changed to thin flakes (9 nm) and ultrathin flakes (less than 4 nm). Confirmed by TEM and Raman characterization (Figs. 3i, j and 2, respectively), the submicronwires and flakes are β - and α - Sb_2O_3 , respectively. This indicates that α - Sb_2O_3 tends to grow under the passivation of Se. To explore the passivation mechanism of Se, we calculated the formation energy of β -(001) plane and α -(111) plane with the increase of Se concentration²⁶.

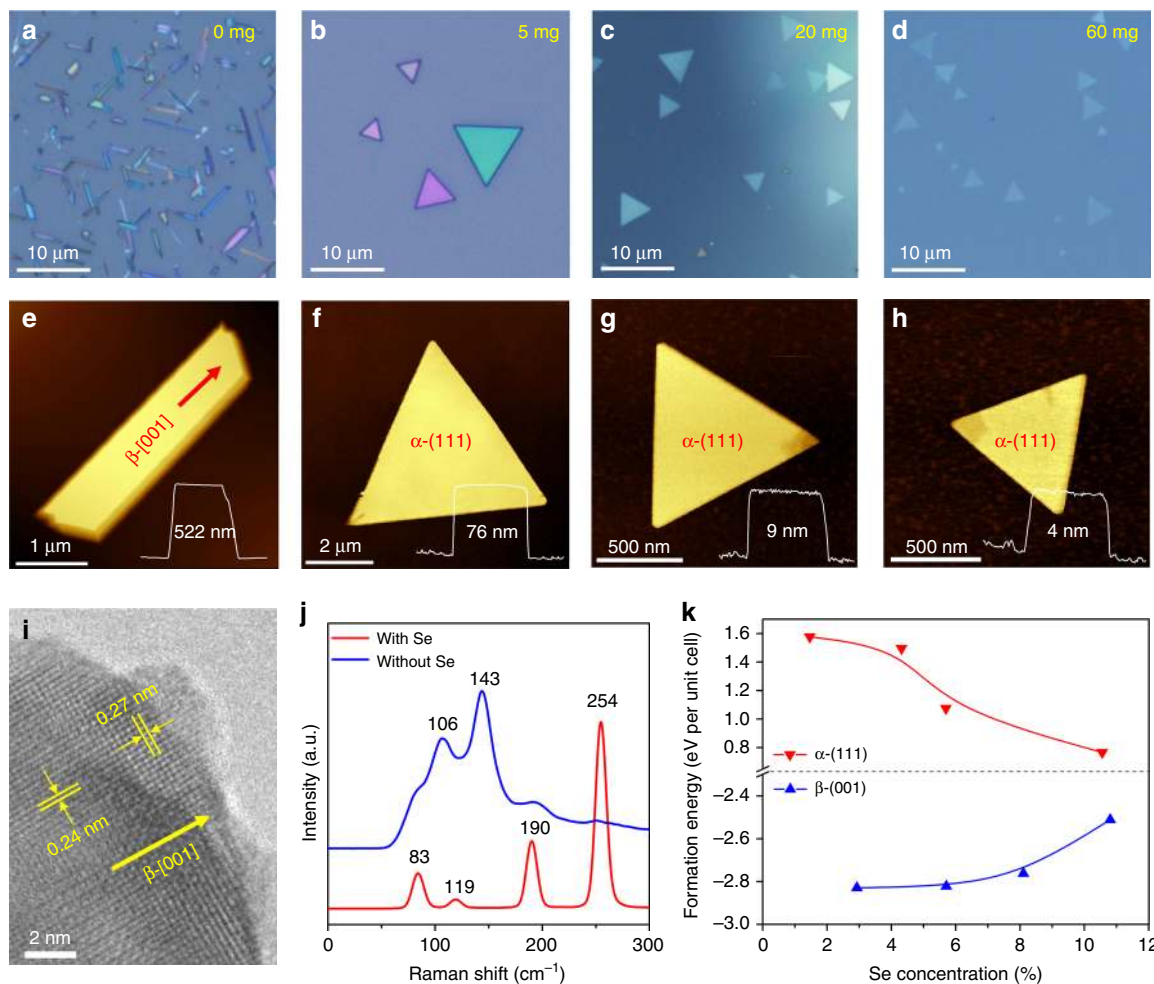


Fig. 3 Morphology and phase evolution of Sb_2O_3 with the amount of Se passivator. **a–h** Typical optical and corresponding AFM images: **a, e** 0 mg; **b, f** 5 mg; **c, g** 20 mg; **d, h** 60 mg. The morphology of Sb_2O_3 is changed as follows: submicrowires \rightarrow thick flakes \rightarrow thin flakes \rightarrow ultrathin flakes. Phase is changed from β (orthorhombic phase) (**a**) to α (cubic phase) (**b–d**). **i** TEM image of the β -phase Sb_2O_3 submicrowire in (**a**) without Se (0 mg); **j** Typical Raman spectra of the submicrowires and flakes. **k** DFT-calculated formation energy of β -(001) plane and α -(111) plane with different concentration of Se passivators, indicating the opposite role played by Se. This relation reveals that the growth of α/β phase is promoted/suppressed with the increase of Se

As shown in Fig. 3k, with the increase of Se concentration, the increased formation energy of β -(001) plane makes the sample unstable, and can hinder (passivate) the 1D growth of Sb_2O_3 . However, for α -(111) plane, the decreased formation energy can make Sb_2O_3 grow favorably on (111) plane with the increase of Se. The above evidence explains why 2D flakes can be obtained under the action of passivator, but does not explain why the thin flakes on (111) plane can be obtained, which is explained by the following calculations.

We compared the surface energies of Sb_2O_3 with specific planes (110) and (111) for α phase and (001) for β phase, as is shown in Fig. 4a, b. In the absence of passivators, the (001) plane in β phase of Sb_2O_3 exhibits the largest surface energy (255 meV per atom), indicating the high activity and bonding tendency for the surface atoms. Actually, fast growth can be obtained for this plane, which leads to the nanorod structural morphology. After using passivators, the gaseous passivator molecules break the dynamic equilibrium. In contrast, the crystal plane (111) of α phase keeps the lower surface energy (38 meV per atom), suggesting the stable surface atomic bonding configuration and slower growth rate. The {110} facets with higher surface energy (73 meV per atom) grow faster (Fig. 4a). As a consequence, the molecular epitaxy mainly occurs along the

{110} planes, resulting in the triangular morphology with (111) top plane for a phase.

As to the situations that Sb_2O_3 is passivated with cationic (In) and anionic (Se, Cl) passivators, we find the distinct structure distortions shown in Fig. 4c, d. The anionic Se and Cl passivators induce significant crystal distortions compared with the cationic In^{27,28}. Such a phenomenon could be understood by the partial density of states and local charge distribution shown in Fig. 4e. The slight wavefunction overlap between anionic passivators and Sb_2O_3 induces strong localized states within the band-gap region, namely shoving up the hybrid orbitals of Se/Cl and Sb_2O_3 , which will break the pristine thermodynamic equilibrium state and suppress the growth of (111) plane. As to the cationic absorbed situation, valence states present diffused distribution and downward movement overall due to the invasion of In passivator into the cage bonding with O atom tightly, which actually destroys the pristine Sb_2O_3 atom stacking configuration^{29,30}.

Phase transitions of 2D Sb_2O_3 molecular crystals. It has been reported that the cubic Sb_2O_3 , denoted as α - Sb_2O_3 , could be transformed into orthorhombic β - Sb_2O_3 (space group $Pccn$, No. 56), which is a reconstructive phase transition from 0D to 1D

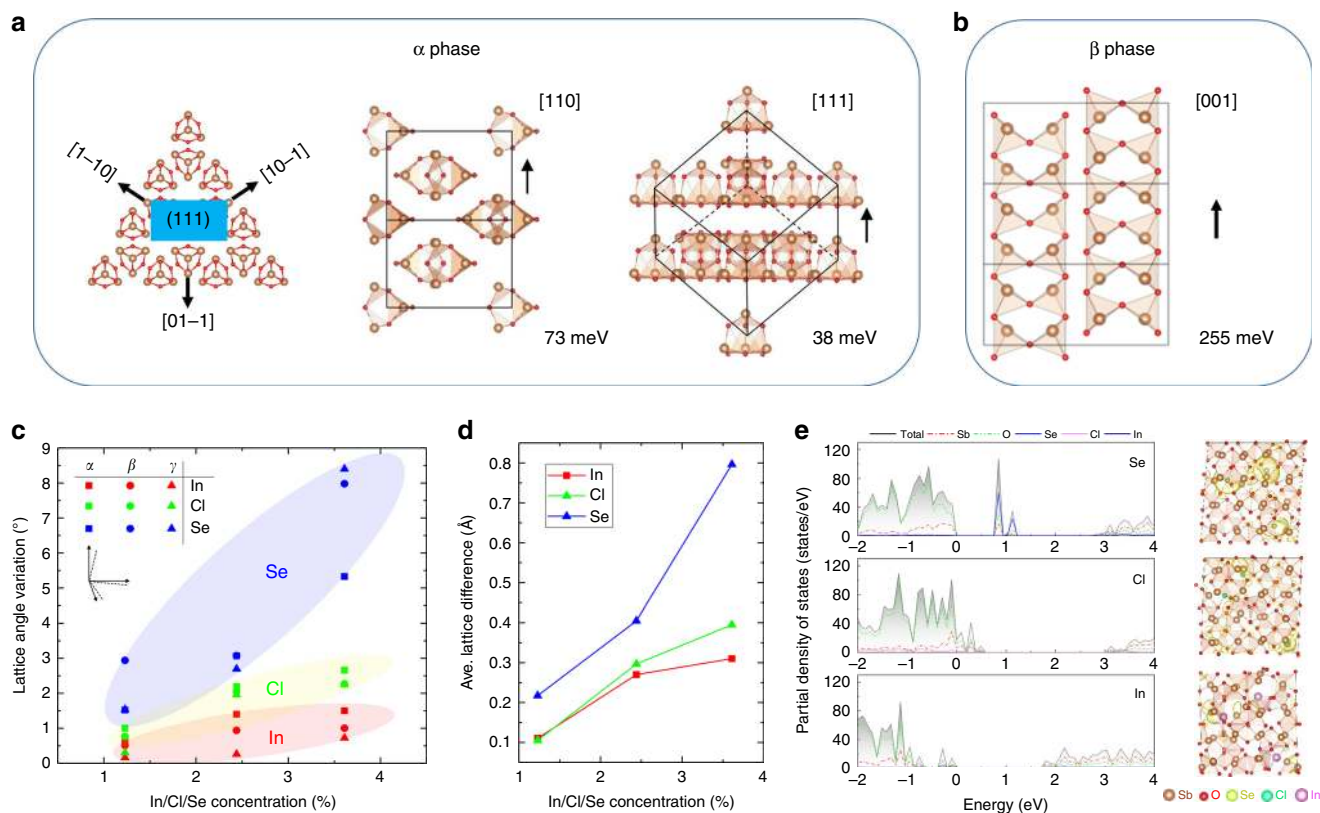


Fig. 4 DFT-calculation of the effect of passivators. **a** Crystallographic preferential growth orientations and surface energy comparison for specific Sb_2O_3 crystal direction (110) and (111) in α phase, and **b** (001) in β phase. Brown balls, Sb atoms. Red balls, O atoms. **c, d** Structural distortions referenced to the pristine Sb_2O_3 , which is described by the variations of crystal angle (α , β , γ) and average lattice differences (Δ_X , $X = \text{Se}$, Cl and In). **e** Partial density of states for Sb_2O_3 with Se, Cl and In absorption on (111) surface and the local charge densities ($\rho = 0.005 \text{ e}\text{Å}^{-3}$). The shaded areas in (**e**) are total density of states

crystal structures³¹. To study the α – β phase transition in Sb_2O_3 flakes, we carried out the temperature-dependent in situ and ex situ Raman characterization with the 532 nm laser excitation. Figure 5a shows the in situ temperature-dependent Raman spectra of a thin Sb_2O_3 flake during heating process from 293 to 673 K with a step of 20 K. Since Sb_2O_3 flakes will sublime above 673 K, no higher temperature is studied³¹. In the temperature range of 293–433 K, only ${}^2\text{F}_{2g}$ and ${}^1\text{A}_g$ peaks of α - Sb_2O_3 are detected. When the temperature rises to 453 K, a new broadening peak appears at 142.7 cm^{-1} , which originates from the A_g mode of β - Sb_2O_3 confirmed by calculated and measured spectra of orthorhombic phase Sb_2O_3 ^{32,33}. In the 453–673 K range, both α and β phases coexist in Sb_2O_3 flake, which is a new mixed phase. The α - Sb_2O_3 flakes start to sublime when heated over 673 K, hindering the complete phase transition to β - Sb_2O_3 . Moreover, A_g , ${}^2\text{F}_{2g}$, and ${}^1\text{A}_g$ peaks all exhibit redshift with temperature linearly (Supplementary Fig. 6), which is due to heat-induced enhanced anharmonic phonon–phonon interactions and thermal dilation³⁴. Meanwhile, with the increase of temperature, the A_g peak first intensifies and then weakens, and similar phenomenon is observed during the cooling process (Fig. 5b). When the temperature drops to 353 K, only ${}^2\text{F}_{2g}$ and ${}^1\text{A}_g$ peaks are left, indicating that the mixed-phase returns to α -phase. This means Sb_2O_3 flake undergoes a partial but reversible phase transition between α and $\alpha + \beta$ mixed-phase with changing temperature. Figure 5c depicts the corresponding 2D Raman intensity maps plot of temperature converted from Fig. 5a, b. The change of peak position, peak intensity and peak shape can be seen more intuitively from these 2D mapping diagrams. In addition to the change of phonon modes, the relative Raman intensity is usually used to

study the extent and hysteresis of structural transitions. As shown in Supplementary Fig. 7, the relative Raman intensity is defined as the ratio of the Raman intensity of the β -phase to the intensity of entire phases³⁵: $R = \beta(\text{A}_g)/[\beta(\text{A}_g) + \alpha(\text{A}_g)]$. In the heating process, R increases first and then decreases, and reaches the maximum of 0.66 at 533 K, but decreases to 0.51 at 673 K, indicating an incomplete transition to β phase. When Sb_2O_3 flake is cooled down, it remains in the mixed-phase until the temperature drops to 353 K, which results in an interesting thermal hysteresis phase transition. To confirm the mixed phases of α and β occurs in the Sb_2O_3 flake, Raman intensity mapping images near 249 cm^{-1} (α - A_g) and 141 cm^{-1} (β - A_g) were taken at 573 K. As depicted in Fig. 5d, e, the triangle morphology of intensity indicates that the mixed phases are uniform in the flake.

It is reported in the literatures that the complete α to β phase transition of bulk Sb_2O_3 appears in the range 829–928 K in different studies³¹, and these temperatures are higher than the sublimation temperature of 2D Sb_2O_3 flakes (693 K) observed in our study. In order to demonstrate the complete phase transition of Sb_2O_3 flakes before their sublimation, we use heat treatment at high temperature for 3 min and then cooling in room temperature to fulfill this transition, because the high temperature phase can be retained during the rapid cooling process (Supplementary Figs. 8–10 and Supplementary Table 1). As shown in Fig. 5f, the ex situ Raman spectra indicate that α -phase can be transformed into β -phase by heat treatment. Below 650 K, there is no obvious phase transition in the sample. When the temperatures of 752 and 807 K are used, the transition from α to a mixed phase is observed. At a higher temperature of 823 K, ${}^2\text{F}_{2g}$ and ${}^1\text{A}_g$ peaks disappear completely, with only the peak at 145 cm^{-1} (β - A_g) left, which

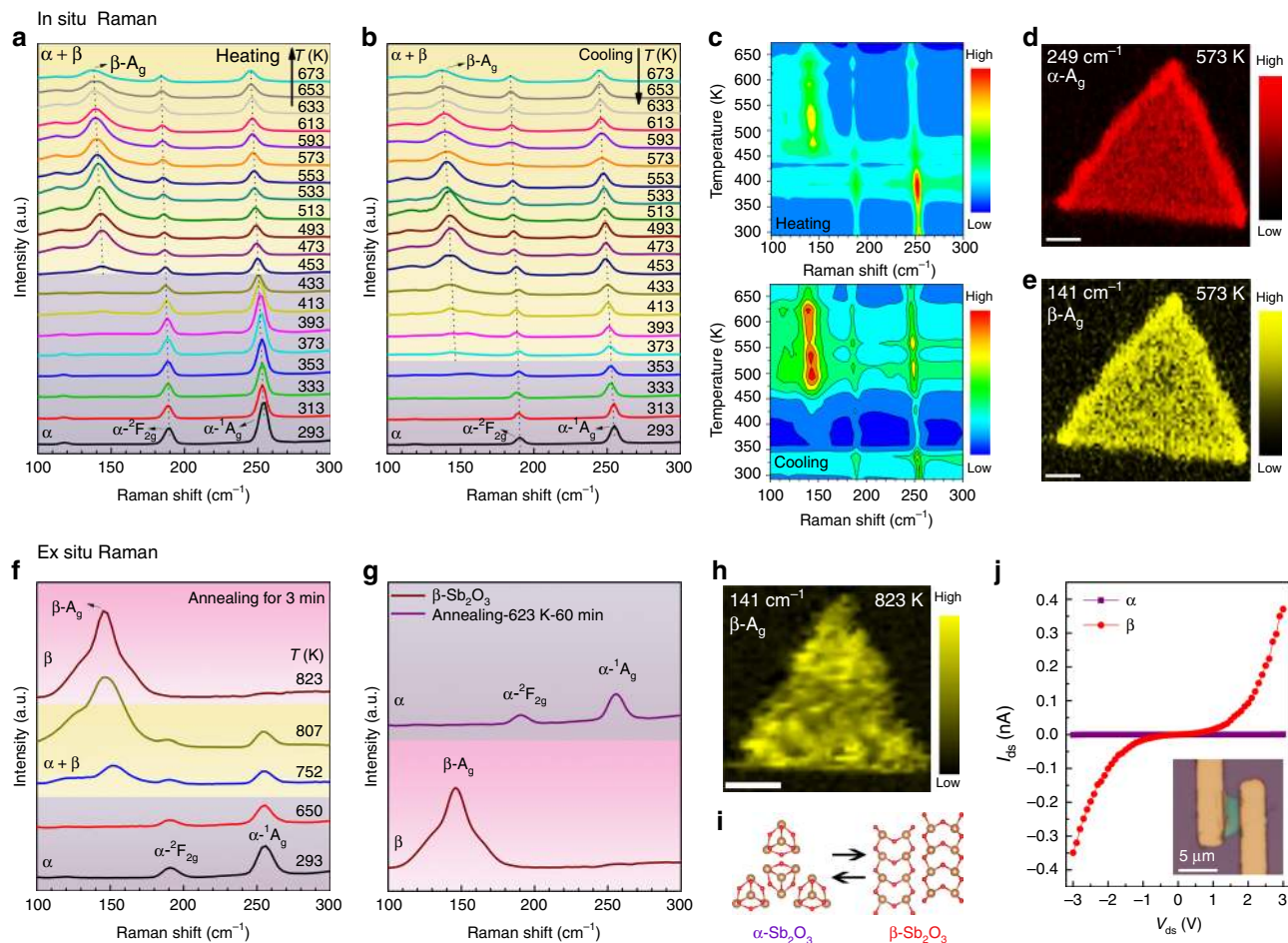


Fig. 5 Heat-induced phase transition in Sb_2O_3 flakes. **a, b** In situ temperature-dependent Raman spectra of a thin $\alpha\text{-Sb}_2\text{O}_3$ flake during heating and cooling processes with the temperature window of 293–673 K. **c** The corresponding 2D Raman intensity maps plot of temperature converted from **(a)** and **(b)**. **d, e** Raman mapping images near 249 cm^{-1} (α -phase) and 141 cm^{-1} (β -phase) taken at 573 K. Scale bar, $2\ \mu\text{m}$. **f** Ex situ Raman spectra of an Sb_2O_3 flake acquired by annealing for 3 min at different temperatures. **g** Raman spectra of the $\beta\text{-Sb}_2\text{O}_3$ flake before and after annealing for 60 min at 623 K. **h** Raman mapping image near 141 cm^{-1} (β -phase) taken after heat treatment at 823 K. Scale bar, $1\ \mu\text{m}$. **i** Ball-and-stick structural models of α - and $\beta\text{-Sb}_2\text{O}_3$. Brown balls, Sb atoms; red balls, O atoms. **j** $I_{\text{ds}}\text{-}V_{\text{ds}}$ curves of the Sb_2O_3 device before (α -phase) and after heat treatment (β -phase). Inset is the optical image of the Sb_2O_3 device

indicates that the sample has achieved the complete transition from α - to β -phase. This thermal-induced phase transition can be expressed as: $\alpha \rightarrow \text{mixed} \rightarrow \beta$. Figure 5g shows the Raman spectra of the $\beta\text{-Sb}_2\text{O}_3$ flake before and after heat treatment for 1 h at 623 K, revealing that the reversible transition from β - to α -phase can be realized by re-annealing. The evolution of phases ($\beta \rightarrow \text{mixed} \rightarrow \alpha$) with annealing time is shown in Supplementary Fig. 11. The triangle shape of Raman intensity mapping near 141 cm^{-1} (β -phase) taken after heat treatment at 823 K in Fig. 5h clearly demonstrates that the original morphology remains unchanged after the transition and the phase transition is complete and uniform (Supplementary Fig. 12). Moreover, the flakes after phase transition can be stable in the air for more than 10 months (Supplementary Fig. 13). Figure 5i shows the structural models of α - and $\beta\text{-Sb}_2\text{O}_3$, which is a transition between 0D Sb_4O_6 molecules and 1D chains of $[\text{SbO}_3]$ trigonal pyramids (Supplementary Fig. 14 and Supplementary Table 2). Phase transition is usually accompanied by the change of properties. In order to explore the changes in electrical properties of Sb_2O_3 flakes, we conducted the $I\text{-}V$ measurements of Sb_2O_3 flake before and after the complete phase transition. The $I_{\text{ds}}\text{-}V_{\text{ds}}$ (I_{ds} , source-drain current; V_{ds} , source-drain voltage) curves of the Sb_2O_3 flake indicate that the conductivity of the device increases by nearly four

orders (at 3 V) after the complete transition of the flake to β -phase via heat treatment at 823 K (Fig. 5j). This insulator-semiconductor transition from α - to β -phase may be attributed to the decrease of band-gaps (3.0 to 2.1 eV, an indirect-direct band-gap transition, Supplementary Figs. 15, 16)³⁰. As discussed above, the anionic (Se, Cl) passivators are critical for the synthesis of 2D Sb_2O_3 crystals. Although most of these passivators could leave the samples in the form of gas phases of dimers or clusters, in the dilute limit there could be isolated passivator atoms left on the as-grown Sb_2O_3 flakes. In the molecular α -phase, the appearance of dilute anionic (Se, Cl) passivators will change a small portion of the Sb_4O_6 cages into cations and keep the crystal insulating. In the nonmolecular β -phase, the anionic (Se, Cl) passivators can be shallow p -type dopants, making the crystal conductive (Supplementary Fig. 17).

In situ TEM observation of $\alpha \rightarrow \beta$ structural transition. In addition to high temperature, electron-beam irradiation (EBI) is another effective method to induce phase transition³⁶. The Sb_2O_3 flakes were transferred onto Si_3N_4 windows in a heating chip for in situ TEM (Supplementary Fig. 18). Figure 6a demonstrates the schematic diagram of EBI on the middle of the Sb_2O_3 flake at room temperature, and the time-dependent in situ TEM images of

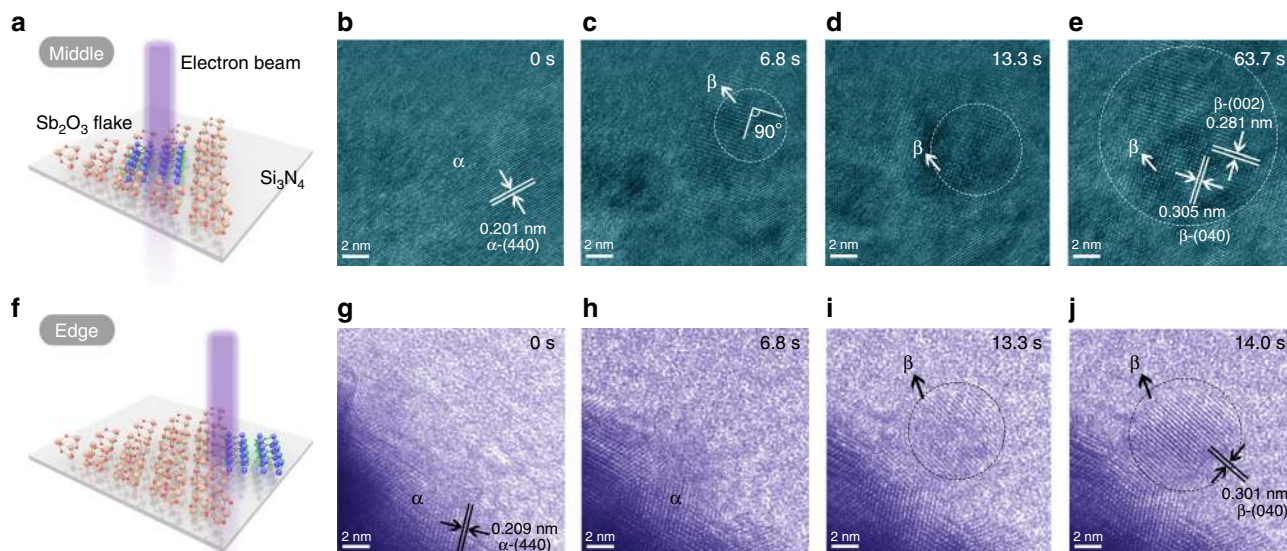


Fig. 6 In situ TEM study of Sb_2O_3 flakes at room temperature. **a** Schematic diagram of electron-beam irradiation on the middle of the Sb_2O_3 flake. α -phase: brown balls for Sb atoms, red balls for O atoms. β -phase: blue balls for Sb atoms, green balls for O atoms. **b–e** Time-resolved HRTEM images reveal the β -phase formation at the middle of the Sb_2O_3 flake; **f** Schematic diagram of electron-beam irradiation on the edge of the Sb_2O_3 flake; **g–j** Time-resolved HRTEM images reveal the β -phase formation at the edge of the Sb_2O_3 flake

β -phase formation are shown in Fig. 6b–e and Supplementary Movie 1. At $t = 0$ s, the flake is α -phase (Fig. 6b). After only 6.8 s of EBI, a nucleation of β -phase appears (marked by white circle in Fig. 6c) and this is the starting point of the phase transition. After 13.3 s of EBI, a transition region of β -phase is obtained (Fig. 6d). As the EBI continues, the region of β -phase increases (marked by white circles). As shown in Fig. 6e, the spacing of the two perpendicular planes is 0.281 and 0.305 nm, corresponding to the β -(002) and (040) planes, respectively. The edge of the material is usually different from the middle of the material, here we use EBI to explore the structural phase transition of the edge of Sb_2O_3 flake (Fig. 6f). Figure 6g–j demonstrates the TEM images of EBI-induced growth of β -phase nanorod at the edge of the Sb_2O_3 flake (Supplementary Movie 2). As a contrast, we compare the images at 6.8 s and find that there is no phase transition at the edge and the phase transition occurs at 13.3 s, which indicates that the phase transition at the edge is slower than that at the middle of the Sb_2O_3 flake (Fig. 6h). After a 13.3 s irradiation, a semi-crystalline rod suddenly appears at the edge (Fig. 6i). At $t = 14.0$ s, the semi-crystalline rod is transformed into a single-crystalline rod, and is connected with the edge, indicating that it grows from the flake (Fig. 6j). The crystal plane spacing is 0.301 nm, which is closest to the (040) plane of β - Sb_2O_3 . This indicates that the flake-nanorod is a heterophase junction fabricated by EBI.

Atomic mechanism of $\alpha \rightarrow \beta$ structural transition in Sb_2O_3 flake. To facilitate phase transition, the flake was heated to 100–350 °C in TEM, providing thermal activation energy for chemical bond rearrangement and atomic migration. Figure 7a–c presents the HRTEM images of the Sb_2O_3 flake at different temperatures. The corresponding atomic models of the $\alpha \rightarrow \beta$ phase transition are illustrated in Fig. 7d–f. The initial Sb_2O_3 lattice (Fig. 7a, d) is α -phase with (111) top plane and the typical angle of the crystal planes is 60°. At 523 K (Fig. 7b), assisted by the EBI, an intermediate phase (denoted β_1) is formed with plane angle of 85° and a phase boundary appears (marked by red dashed line). This phase boundary is also observed in the EBI-induced transition at room temperature (Supplementary Fig. 19). From the arrangement of atomic columns near the red dashed

line, it can be seen that they are not in a straight line, and there are dislocations and defects, which indicates that migration and rearrangement of atoms exist at the boundary. At a higher temperature of 623 K, β -phase is observed and the angle between the two planes is changed to 90° (Fig. 7c, f). This cubic/orthorhombic transition comes from the breakage and recombination of Sb–O–Sb chemical bonds (both α and β phases have six Sb–O bonds per formula unit), which is a typical reconstructive phase transition. From the transformation of plane angles 60° \rightarrow 85° \rightarrow 90°, we can speculate a possible mechanism of this $\alpha \rightarrow \beta$ reconstructive phase transition which consists of: (i) nucleation of the intermediate phase β_1 (Fig. 7b and Supplementary Fig. 20), (ii) migration and rearrangement of Sb and O atoms (Fig. 7e), and (iii) migration of boundaries and growth of β -phase (Fig. 7c). Figure 7e shows the schematic model of migration of atoms near the boundary, and the blue line represents the migrated atomic column, and the blue arrows represent the direction of migration. The migration of Sb atoms from A site to B site (blue letter labeled in Fig. 7e) can increase the angle of the typical crystal planes and lead to the appearance of β_1 -phase. As a consequence, a β -phase forms, as shown in Fig. 7c. For reconstructive structural phase transition, in addition to angle changes, the spacing and mismatch will also change regularly³⁷. Lattice mismatch is given by the expression: $\delta = \frac{|D_\beta - D_\alpha|}{D_\alpha} = \frac{\Delta D}{D_\alpha}$ where δ is the relative difference of atomic distance (D_α and D_β) between two adjacent phases. The parameters during the phase transition are listed in Supplementary Table 3. When δ is between 0.05 and 0.25, a semi-coherent interface is formed ($\delta = 0.084$ in Fig. 7b), which needs dislocations to release the elastic strain energy and achieves the partial matching of atoms in two phases³⁸.

To conclude, we have prepared ultrathin 2D Sb_2O_3 inorganic molecular crystals with thickness down to monolayer by PAVD. The passivator can suppress the heterophase growth, and promote the lateral growth of Sb_2O_3 molecular crystals along the high-energy crystal planes. The thermal-induced phase transition of Sb_2O_3 flakes is reversible between α - and mixed-phase with a thermal hysteresis loop. The reversible switching between α - and β -phases can be controlled by annealing. Moreover, α -phase can be transformed into β -phase under electron-beam irradiation at

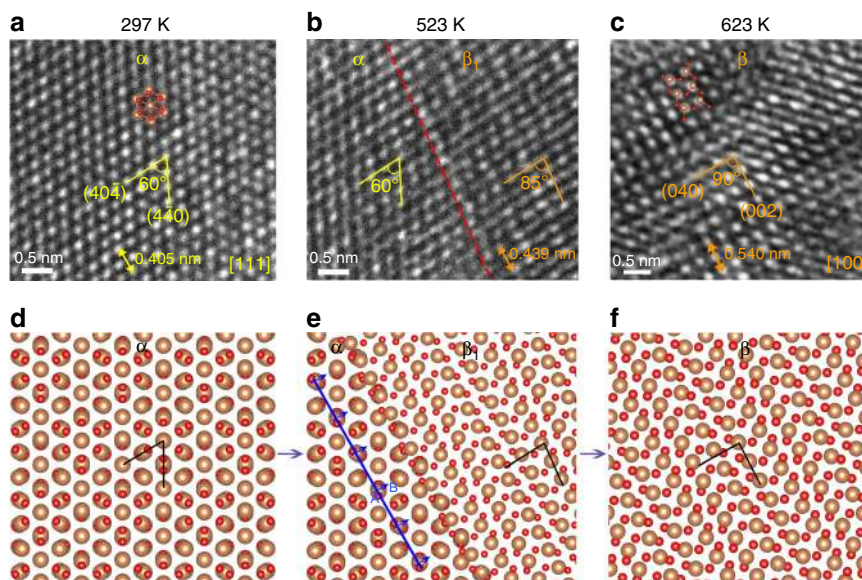


Fig. 7 Atomic mechanism of structural evolution in Sb_2O_3 flake at elevated temperatures. **a** HRTEM image of α -phase with (111) top plane at room temperature. **b** At 523 K, an intermediate phase forms (denoted β_1) with plane angle of 85° and a phase boundary appears. **c** At 623 K, β -phase forms with plane angle of 90° and top plane of (100). **d–f** Atomic models of the $\alpha \rightarrow \beta$ phase transition corresponding to the TEM images in (a–c), respectively

room and high temperature. During this reconstructive phase transition, structural change attributes to the nucleation of the intermediate phase and migration of boundaries. This investigation on 2D Sb_2O_3 could be a promoter for the discovery of new 2DIMCs and future phase-change devices.

Methods

Growth of 2D Sb_2O_3 flakes. The 2D Sb_2O_3 flakes were grown by van der Waals epitaxy methods (Route 1 and Route 2) in a three-zone CVD tube furnace (Thermcraft). In Route 1, 300 mg of $\text{SbCl}_3 \cdot x\text{H}_2\text{O}$ (99.9%, Macklin), 15 mg of InCl_3 (99.999%, Alfa), and fresh mica ($\text{KMg}_3\text{AlSi}_3\text{O}_{10}\text{F}_2$) sheets were put in the zone 1 ($T_1 = 320^\circ\text{C}$), zone 2 ($T_2 = 700^\circ\text{C}$), and zone 3 ($T_3 = 400^\circ\text{C}$), respectively. Ar (60 sccm) was used as carrier gas and the synthesis process was maintained for 45 min. In Route 2, 67 mg of Se (99.999%, Alfa), 40 mg of Sb_2O_3 (99.999%, Alfa), and fresh mica sheets were put in the zone 1 ($T_1 = 280^\circ\text{C}$), zone 2 ($T_2 = 650^\circ\text{C}$), and zone 3 ($T_3 = 400^\circ\text{C}$), respectively. Mica substrates were located about 22–26 cm from the center of zone 2. Ar (80 sccm) was used as carrier gas and the synthesis process was maintained for 20 min at ambient pressure. Then the furnace was cooled down to room temperature under the Ar flow.

Transfer process of 2D Sb_2O_3 flakes. The Sb_2O_3 flakes grown on micas were transferred onto TEM Cu grids and SiO_2/Si substrates by a water-boiling method. First, the poly (methyl methacrylate) (PMMA) was spin-coated onto the mica substrate with as-grown samples at 3000 rpm for 1 min, and then baked at 150°C for 5 min. The above process was repeated for three times to obtain a thick robust PMMA membrane on the substrate. Second, the PMMA/mica was put into a 100 ml beaker containing 50 ml of deionized water and heated for 1.5 h at 190°C . Then, the PMMA membrane with Sb_2O_3 flakes was peeled off slowly from the mica substrate by tweezers, and attached to Cu grids or SiO_2/Si substrates. Finally, the PMMA/ Sb_2O_3 was baked at 100°C for 5 min, and then the PMMA was completely removed in acetone.

Heat treatment. We used a home-made slide furnace for rapid annealing heat treatment (Supplementary Fig. 7). Before heating, the α - Sb_2O_3 flakes were placed in a quartz tube and outside the heating zone. After the Ar flow washing for an hour, the furnace temperature was increased to the specified temperature at $30^\circ\text{C}/\text{min}$, then the heating zone was moved to the sample position quickly for rapid heating-up to the set temperature. The actual rapid annealing temperature is defined as the maximum temperature obtained by the sample (Supplementary Fig. 9). After heating for 3 min, the heating zone was moved away from the sample position. The sample was cooled to room temperature in 20 min in Ar flow (heating and cooling rates see Supplementary Table 1). For complete phase transition, the heating rate and cooling rate are 173.3 and 56.2 K/min, respectively. For slow annealing heat treatment, β - Sb_2O_3 flakes were slowly heated to 573–623 K at a rate of 20 K/min, then kept for 60 min, and finally cooled to room temperature at a rate of 1 K/min.

Materials characterizations. The Sb_2O_3 flakes were characterized by OM (Olympus BX51), AFM (Bruker Dimension icon), Raman spectroscopy (WITec Alpha300 Raman and Horiba LabRAM HR800, excitation wavelength of 532 nm), and TEM (FEI Tecnai G2 F30, acceleration voltage of 300 kV). High temperature Raman spectra were collected by $\times 50$ objective lens. Linkam THMS600 and TS1000EV heating stages were used to control the temperature of the sample. The laser power at the top of the stage window is 20–25 mW, correspondingly, the power on the surface of the sample is much smaller. STEM-HAADF images were recorded using Cs-corrected Titan Cubed Themis G2 300 and JEOL JEM-ARM 200 F with acceleration voltage of 200 kV.

Device fabrication and measurement. The devices were fabricated by electron-beam lithography (EBL, FEI Quanta 650 SEM, and Raith Elphy Plus) and laser direct-write lithography (LDWL, DMO MicroWriter ML Baby), and then Cr/Au (5 nm/100 nm) metal contacts were deposited using thermal evaporation (Nexdep, Angstrom Engineering). The electrical properties were measured using a semiconductor device analyzer (Keithley 4200-SCS) in a probe station (Lake Shore CRX-6.5K).

In situ TEM. The heating holder from DENS solutions was used for in situ heating experiments in a high-resolution TEM (FEI Talos F200X) operated at 200 kV. The Sb_2O_3 flakes were transferred onto silicon nitride windows in a heating chip (Wildfire Nanochip) by the PMMA-assisted method. Before in situ TEM experiments, the samples were cleaned with argon plasma for 30 s to remove the residual PMMA and impurities on the surface. The heating rate of the whole process was set to $10^\circ\text{C}/\text{min}$. During the in situ experiments, the electron-beam current was kept at 50–100 pA.

DFT calculations. DFT calculations were performed using the Vienna Ab Initio Simulation Package (VASP)^{39,40}. The generalized gradient approximation with the Perdew–Burke–Ernzerhof exchange–correlation functional (GGA-PBE)⁴¹ were used with a 500 eV cut-off energy to expand the electronic wave functions. All the systems with free crystal lattices experienced fully atomic relaxation by the conjugate gradient (CG) algorithm until the residual forces and maximum energy difference were less than 5×10^{-3} eV and 10^{-6} eV/Å. Van der Waals corrections of optB88-vdW functional^{42,43} was considered for dispersion forces, which guarantee the accuracy of structural parameters (the crystal lattice error between theory and experiment is within 0.045%). The Monkhorst-Pack k -point meshes of $4 \times 4 \times 4$ and $4 \times 4 \times 1$ for Sb_2O_3 bulk and 2D flakes with (110) and (111) planes in Brillouin zone were employed. In our study, the passivator molecules were interacted with the surface atoms and molecules of Sb_2O_3 randomly with increasing concentrations to simulate the experiment process. All the crystal structures and charge densities were drawn using the VESTA software⁴⁴.

Data availability

All relevant data are either supplied in the paper and Supplementary Information, or available from the authors upon request.

Received: 16 February 2019; Accepted: 10 September 2019;

Published online: 17 October 2019

References

- Ong, W.-L. et al. Orientational order controls crystalline and amorphous thermal transport in superatomic crystals. *Nat. Mater.* **16**, 83–88 (2017).
- Lovat, G. et al. Room-temperature current blockade in atomically defined single-cluster junctions. *Nat. Nanotech.* **12**, 1050–1054 (2017).
- Clement, N. & Fujiwara, A. Molecular diodes: breaking the Landauer limit. *Nat. Nanotech.* **12**, 725–726 (2017).
- Chen, X. et al. Molecular diodes with rectification ratios exceeding 10^5 driven by electrostatic interactions. *Nat. Nanotech.* **12**, 797–803 (2017).
- Cui, L. et al. Peltier cooling in molecular junctions. *Nat. Nanotech.* **13**, 122–127 (2018).
- Cinchetti, M., Dediú, V. A. & Hueso, L. E. Activating the molecular spinterface. *Nat. Mater.* **16**, 507–515 (2017).
- Atesci, H. et al. Humidity-controlled rectification switching in ruthenium-complex molecular junctions. *Nat. Nanotech.* **13**, 117–121 (2018).
- Smits, E. C. P. et al. Bottom-up organic integrated circuits. *Nature* **455**, 956–959 (2008).
- Claridge, S. A. et al. Cluster-assembled materials. *ACS Nano* **3**, 244–255 (2009).
- Sun, X. et al. A molecular spin-photovoltaic device. *Science* **357**, 677–680 (2017).
- Yin, J. et al. Molecular behavior of zero-dimensional perovskites. *Sci. Adv.* **3**, e1701793 (2017).
- He, D. et al. Two-dimensional quasi-freestanding molecular crystals for high-performance organic field-effect transistors. *Nat. Commun.* **5**, 5162 (2014).
- Lu, J. et al. Transforming C_{60} molecules into graphene quantum dots. *Nat. Nanotech.* **6**, 247–252 (2011).
- Lee, K. et al. Two-dimensional fullerene assembly from an exfoliated van der Waals template. *Angew. Chem. Int. Ed.* **57**, 6125–6129 (2018).
- Zhang, Z. et al. Robust epitaxial growth of two-dimensional heterostructures, multiheterostructures, and superlattices. *Science* **357**, 788–792 (2017).
- Sahoo, K. P. et al. One-pot growth of two-dimensional lateral heterostructures via sequential edge-epitaxy. *Nature* **553**, 63–67 (2018).
- Zhou, J. et al. A library of atomically thin metal chalcogenides. *Nature* **556**, 355–359 (2018).
- Li, S. et al. Vapour–liquid–solid growth of monolayer MoS_2 nanoribbons. *Nat. Mater.* **17**, 535–542 (2018).
- Vlassiok, I. V. et al. Evolutionary selection growth of two-dimensional materials on polycrystalline substrates. *Nat. Mater.* **17**, 318–322 (2018).
- Wu, J. et al. Preparation of single-crystalline heterojunctions for organic electronics. *Adv. Mater.* **29**, 1606101 (2017).
- Pereira, A. L. J. et al. Structural and vibrational study of cubic Sb_2O_3 under high pressure. *Phys. Rev. B* **85**, 174108 (2012).
- Costa, L. et al. Thermal behaviour of chlorine-antimony fire-retardant systems. *Polym. Degrad. Stab.* **30**, 13–28 (1990).
- Svensson, C. Refinement of the crystal structure of cubic antimony trioxide, Sb_2O_3 . *Acta Cryst.* **B31**, 2016–2018 (1975).
- Saitoh, A. Raman scattering, luminescence, and absorption edge under hydrostatic pressures of layered BiI_3 and SbI_3 . *J. Raman Spectrosc.* **38**, 537–542 (2007).
- Li, H. et al. From bulk to monolayer MoS_2 : evolution of Raman scattering. *Adv. Funct. Mater.* **22**, 1385–1390 (2012).
- Liu, L. et al. Phase-selective synthesis of 1T' MoS_2 monolayers and heterophase bilayers. *Nat. Mater.* **17**, 1108–1114 (2018).
- Jin, B. et al. Self-limited epitaxial growth of ultrathin nonlayered CdS flakes for high-performance photodetectors. *Adv. Funct. Mater.* **28**, 1800181 (2018).
- Hu, X. et al. Halide-induced self-limited growth of ultrathin nonlayered Ge flakes for high-performance phototransistors. *J. Am. Chem. Soc.* **140**, 12909–12914 (2018).
- Carey, J. et al. The electronic structure of the antimony chalcogenide series: Prospects for optoelectronic applications. *J. Solid State Chem.* **213**, 116–125 (2014).
- Allen, J. P. et al. Electronic structures of antimony oxides. *J. Phys. Chem. C* **117**, 14759–14769 (2013).
- Orman, R. G. & Holland, D. Thermal phase transitions in antimony (III) oxides. *J. Solid State Chem.* **180**, 2587–2596 (2007).
- Voit, E. I. et al. Vibrational spectroscopic and quantum chemical study of antimony (III) oxide. *J. Struct. Chem.* **50**, 60–66 (2009).
- Deng, Z. T. et al. Synthesis and purple-blue emission of antimony trioxide single-crystalline nanobelts with elliptical cross section. *Nano Res.* **2**, 151–160 (2009).
- Li, L. et al. Strong in-plane anisotropies of optical and electrical response in layered dimetal chalcogenide. *ACS Nano* **11**, 10264–10272 (2017).
- Wang, Y. et al. Structural phase transition in monolayer $MoTe_2$ driven by electrostatic doping. *Nature* **550**, 487–491 (2017).
- Lin, Y. C. et al. Atomic mechanism of the semiconducting-to-metallic phase transition in single-layered MoS_2 . *Nat. Nanotech.* **9**, 391–396 (2014).
- Dmitriev, V. P. et al. Definition of a transcendental order parameter for reconstructive phase transitions. *Phys. Rev. Lett.* **60**, 1958–1961 (1988).
- Han, Y. et al. Sub-nanometre channels embedded in two-dimensional materials. *Nat. Mater.* **17**, 129–133 (2018).
- Kresse, G. & Hafner, J. Ab initio molecular dynamics for liquid metals. *Phys. Rev. B* **47**, 558–561 (1993).
- Kresse, G. & Furthmüller, J. Efficient iterative schemes for ab initio total-energy calculations using a plane-wave basis set. *Phys. Rev. B* **54**, 11169–11186 (1996).
- Perdew, J. P., Burke, K. & Ernzerhof, M. Generalized gradient approximation made simple. *Phys. Rev. Lett.* **77**, 3865–3868 (1996).
- Klimeš, J., Bowler, D. R. & Michaelides, A. Chemical accuracy for the van der Waals density functional. *J. Phys. Condens. Matter* **22**, 022201 (2010).
- Klimeš, J., Bowler, D. R. & Michaelides, A. Van der Waals density functionals applied to solids. *Phys. Rev. B* **83**, 195131 (2011).
- Momma, K. & Izumi, F. VESTA 3 for three-dimensional visualization of crystal, volumetric and morphology data. *J. Appl. Crystallogr.* **44**, 1272 (2011).

Acknowledgements

We thank J. Luo and W. Xi from Tianjin University of Technology for in situ TEM measurements, data analysis and helpful discussions. This work was supported by the National Natural Science Foundation of China (Grant Nos. 21825103, 51727809, 11774239 and 11804230), Hubei Provincial Natural Science Foundation of China (2019CFA002), the Project funded by China Postdoctoral Science Foundation (Grant No. 2018M642832), and the Fundamental Research Funds for the Central University (Grant No. 2019kfyXMBZ018). The authors also acknowledge the technical support from the Analytical and Testing Center of Huazhong University of Science and Technology. Y.C. acknowledges the support from the Department of Energy, Office of Basic Energy Sciences, Division of Materials Science and Engineering under contract DE-AC02-76SF00515.

Author contributions

T.Z. and Y.C. conceived the original idea and supervised the research project. W.H. conducted the growth, OM, Raman, AFM, IV, and TEM of 2D crystals. The devices were fabricated by W.H. with L.L. and F.W.'s help. P.H. and X. Zhang carried out DFT calculations and performed the detailed theoretical analysis. P.L. participated in drawing the schematic diagrams. The manuscript was written by W.H., K.L., P.H., X. Zhang, T.Z. and Y.C. with input from the other authors. X. Zhou and H.L. discussed the results and commented on the manuscript.

Competing interests

The authors declare no competing interests.

Additional information

Supplementary information is available for this paper at <https://doi.org/10.1038/s41467-019-12569-9>.

Correspondence and requests for materials should be addressed to Y.C. or T.Z.

Peer review information *Nature Communications* thanks the anonymous reviewer(s) for their contribution to the peer review of this work. Peer reviewer reports are available.

Reprints and permission information is available at <http://www.nature.com/reprints>

Publisher's note Springer Nature remains neutral with regard to jurisdictional claims in published maps and institutional affiliations.



Open Access This article is licensed under a Creative Commons Attribution 4.0 International License, which permits use, sharing, adaptation, distribution and reproduction in any medium or format, as long as you give appropriate credit to the original author(s) and the source, provide a link to the Creative Commons license, and indicate if changes were made. The images or other third party material in this article are included in the article's Creative Commons license, unless indicated otherwise in a credit line to the material. If material is not included in the article's Creative Commons license and your intended use is not permitted by statutory regulation or exceeds the permitted use, you will need to obtain permission directly from the copyright holder. To view a copy of this license, visit <http://creativecommons.org/licenses/by/4.0/>.

© The Author(s) 2019